MNRAS 000, 1–14 (2019) Preprint 17 May 2019 Compiled using MNRAS LaTeX style file v3.0

On the Comparison of AGN with GRMHD Simulations: I. Sgr A*

Richard Anantua,[1,2,3⋆] Sean Ressler[1,4], Eliot Quataert[1,4]
[1] *Astronomy Department, Theoretical Astrophysics Center, University of California, Berkeley, 601 Campbell Hall, Berkeley, CA 94720-3411, USA*
[2] *Center for Astrophysics | Harvard & Smithsonian, 60 Garden Street, Cambridge, MA 02138, USA*
[3] *Black Hole Initiative at Harvard University, 20 Garden Street, Cambridge, MA 02138, USA*
[4] *Department of Physics, University of California Berkeley, 1 LeConte Hall, Berkeley, CA 94720-3411, USA*

Accepted XXX. Received YYY; in original form ZZZ

ABSTRACT
We present models of Galactic Center emission in the vicinity of Sagittarius A* that use parametrizations of the electron temperature or energy density. These models include those inspired by two-temperature general relativistic magnetohydrodynamic (GRMHD) simulations as well as jet-motivated prescriptions generalizing equipartition of particle and magnetic energies. From these models, we calculate spectra and images and classify them according to their distinct observational features. Some models produce morphological and spectral features, e.g., image sizes, the sub-mm bump and low frequency spectral slope compatible with observations. Models with spectra consistent with observations produce the most compact images, with the most prominent photon rings. Limb brightened outflows are also visible in many models. Of all the models we consider, that which represents the current data the best is one in which electrons are relativistically hot when magnetic pressure is larger than the thermal pressure, but cold (i.e., negligibly contributing to the emission) otherwise. This work is part of a series also applying the "observing" simulations methodology to near-horizon regions of supermassive black holes in M87 and 3C 279.

Key words: Accretion Disks – MHD – Black Holes

1 INTRODUCTION

Merely $d = 8.18$ kpc away (Abuter et al. 2019) at the Galactic Center, Sagittarius A* (Sgr A*) is the best known accreting supermassive black hole. With $m_{\rm BH} = 4.14$ million solar masses (Abuter et al. 2019) (subtending 5.3 μas at Earth), Sgr A* is a prime candidate for the next measurement of a black hole shadow by the Event Horizon Telescope (EHT, Doeleman et al. 2008)– after M87's. In April 2019, the EHT imaged emission around the center of the giant elliptical galaxy M87, finding a 42 μas-wide annulus with a Southern excess consistent with relativistic predictions of beamed emission in the Kerr metric of a 6.5 billion solar mass black hole (Event Horizon Telescope Collaboration et al. 2019a). The distribution of flux density over the EHT M87 image– along with a conservative lower bound on the jet power of $L_{\rm M87} \geq 10^{42}$ erg/s– precludes models with a non-spinning black hole, supporting the interpretation of the M87 jets as powered by the Blandford-Znajek mechanism (Blandford & Znajek 1977). Image reconstruction of Sgr A* data has presented unique challenges relative to that for M87 due to the dynamical timescales of minutes as opposed to days (Event Horizon Telescope Collaboration et al. 2019a). GRAVITY (Gillessen et al. 2010) has recently measured astrometrically the proper motion of several "hot spots" (i.e., near infrared flares) orbiting the Galactic Center black hole at $\sim 6-10$ gravitational radii ($M \equiv r_g = Gm_{\rm BH}/c^2$), suggesting that the innermost accretion flow may be relatively face on and strongly magnetized (Gravity Collaboration et al. 2018). These horizon-scale probes of plasma physics, accretion physics, and strong general relativistic effects provide strong constraints on theoretical models.

Incorporating all these effects into analytic models is difficult, and thus General Relativistic Magnetohydrodynamic (GRMHD) simulations are the most promising avenues for theoretical modeling (Gammie et al. 2003a; Sądowski et al. 2014; White et al. 2016; Porth et al. 2017). These simulations solve the equations of MHD in the Kerr metric for a rotating black hole in 3+1 dimensions, naturally capturing the magnetorotational instability (MRI), the formation of jets, turbulence, and general relativistic effects.

As an especially low-luminosity active galactic nucleus

⋆ E-mail: ranantua@cfa.harvard.edu

(LLAGN), the dynamical time for accretion in Sgr A* is much shorter than the electron-ion Coulomb collision time. This means that the flow can roughly be described as a two-temperature plasma (Mahadevan & Quataert 1997) and that information beyond that provided by the standard GRMHD equations is needed to constrain the electron temperature, a key parameter in emission modeling. Many approaches have been taken in the literature for setting the electron temperature. Simple post-processing prescriptions that "paint on" electron temperatures, such as those that set a constant electron-to-proton temperature ratio (Mościbrodzka et al. 2009) everywhere or that set the electron temperature to be some function of plasma parameters (Shcherbakov et al. 2012; Mościbrodzka & Falcke 2013; Chan et al. 2015), are useful for rapidly and directly connecting observations to model parameters. More sophisticated treatments directly evolve the electron temperature alongside the single-fluid equations of GRMHD and incorporate knowledge of electron/ion heating gained from particle-in-cell (PIC) simulations of collisionless plasmas (Ressler et al. 2015, 2017; Sądowski et al. 2017; Chael et al. 2018). Though these models are more physically motivated and self-consistent, they are more expensive to run which makes it difficult to fully explore the parameter space of electron temperature spanned by our uncertainty in the dominant mechanism of electron/ion heating. Furthermore, conservative GRMHD simulations are unable to properly model the thermodynamics of flows in which the magnetic energy density far exceeds the rest mass energy density (as it often does in the jet). Thus, two-temperature simulations that rely on an accurate calculation of the total fluid heating rate cannot be trusted in these regions; parametric models that depend only on the more reliable local magnetic energy density may be more appropriate there.[1]

Given this uncertainty, we consider it instructive to further explore the dependence of the spectra and near-horizon-scale images of Sgr A* on different post-processing models of the electron temperature. In doing so, we include not only some of the prescriptions used in past work to model the Galactic Center, but also those attempting to mimic the qualitative behavior seen in recent two-temperature GRMHD simulations and those successfully used to model other systems, (e.g., Blandford & Königl 1979; Blandford & Anantua 2017; Anantua et al. 2018). We synthesize our results by categorizing the synthetic images and spectra into a small number of groups according to their emission physics. This program adds to the foundation of efforts at classifying and understanding jet (or outflow)/accretion disk/black hole (JAB) emission through a unified framework flexible enough to model disk, corona and outflow or jet regions with a small set of parameters– a methodology we call "Observing" JAB Simulations.

This paper is structured as follows: Section 2 is a brief synopsis of the observations of Sgr A* used to constrain our models; Section 3 describes the numerical simulations used in this work; Section 4 presents models for the accretion flow, electron temperature and emission; Section 5 provides results: images and spectra for the models; Section 6 compares the models in three different simulations to each other and to observations, resulting in a classification distilling various model morphologies, sizes and spectral shapes into four types; and Section 7 concludes.

In what follows, the speed of light, c, and the Boltzmann constant, k_B, are set to unity. Charge neutrality requires the electron number density, n_e, to be $\approx$ the proton number density, $n_p \equiv n_0$. Then, the mass density is $\rho \approx \rho_p = m_p n_0$, where m_p is the mass of a proton. Setting m_p to 1 gives $P_e = \rho T_e$. The total temperature, $T_{\rm tot} = T_e + T_p$ is given by the simulation; T_e is modeled.

2 OBSERVATIONS

Sgr A* has been observed for many years now in the radio, mm, infrared, and X-rays (Fish et al. 2011; Neilsen et al. 2013; Bower et al. 2015; Gravity Collaboration et al. 2018). Time variability tends to increase with frequency, with the radio emission being the most stable and the infrared and X-ray emission showing frequent occurrence of large amplitude flares, likely caused by nonthermal particle acceleration. Since we consider only thermal emission in this work, we treat the 10% of the quiescent X-ray flux estimated to originate close to the black hole (Neilsen et al. 2013) as an upper limit. For a comprehensive list of the observational data points used in this work as constraints on our models (and plotted alongside our model spectra), see Ressler et al. (2017).

Additionally (as a constraint on our model images) we use the intrinsic size limit of the emitting region set by EHT of 37^{+16}_{-10} μas (Doeleman et al. 2008). This size is calculated as the FWHM of the best fit circular Gaussian to the observation. Recent Sgr A* measurements of non-zero closure phase, e.g., $5.0^{\circ}{}^{+12.9^{\circ}}_{-4.6^{\circ}}$ from measurements along the SMT-CARMA-APEX triangle (Lu et al. 2018), rule out a spherically symmetric emission profile. However, this should not be critical for size constraint comparisons in this work in which synthetic images tend to differ by orders of magnitude in size and also tend to differ markedly in shape.

3 PRINCIPAL GRMHD SIMULATIONS

We perform a set of three simulations using the conservative, 3D, ideal GRMHD code `HARM` (Gammie et al. 2003a), which we denote as Standard and Normal Evolution (SANE), Magnetically Arrested Disc (MAD) and semi-MAD. The simulations all have dimensionless spin $a = 0.5$, start from a Fishbone & Moncrief (1976) torus, and have resolutions of 320 x 256 x 64, uniform in the coordinates $x_1(r,\theta), x_2(r,\theta)$, and $x_3 \equiv \varphi$, that are "cylindrified" and hyper-exponentiated (Tchekhovskoy et al. 2011) versions of $h = 0.3$ modified Kerr-Schild (MKS) coordinates (Gammie et al. 2003a), a process which is described in Appendix B of Ressler et al. (2017). MKS coordinates focus resolution towards the midplane of the simulation, the "cylindrification" process increases the angular width of cells with $r \lesssim 10M$, while

[1] This may be part of the reason why two-temperature GRMHD simulations of Sgr A* have thus far under-produced the low frequency radio emission of Sgr A* (Ressler et al. 2017; Chael et al. 2018), as that emission is often assumed to be powered by the magnetized outflow. Alternatively, a small population of non-thermal particles can also explain the $\sim$ flat low frequency radio spectrum (Özel et al. 2000; Yuan et al. 2002).

the hyper-exponentiation extends the radial extent of the grid to thousands of r_g by rapidly increasing the radial size of cells at $r > 400M$. Where the three simulations differ is in both the size of the initial torus and the geometry of the initial magnetic field contained within this torus. The SANE initial torus has an inner boundary of $r_{\rm in} = 12M$ and pressure maximum at $r_{\rm max} = 24M$, while the semi-MAD and MAD initial tori have inner radii of $r_{\rm in} = 15M$ and pressure maxima at $r_{\rm max} = 34.5M$. The magnetic vector potential scales as $A_\phi \propto \rho$ in the SANE case and $A_\phi \propto r^4\rho^2$ in the semi-MAD case, both of which we normalize such that $\max(P)/\max(P_B) = 100$. The MAD vector potential is more complicated and is computed as described in Tchekhovskoy et al. (2011) while we normalize it such that $\min(P/P_B) = 100$. The resulting steady-state, time-averaged magnetic flux threading the horizon, Φ_{BH}, for each of the runs are $\ll 1\ M\sqrt{\dot{m}c}$ (SANE), $\approx 40\ M\sqrt{\dot{m}c}$ (semi-MAD), and $\approx 50\ M\sqrt{\dot{m}c}$ (MAD).

The simulations implement the numerical density floor prescription $u_e \geq 0.01u_g$ from Ressler et al. (2015). The simulation grid concentrates 3D spatial resolution in the disk, allowing for non-axisymmetric turbulence, kink instabilities, etc. in the MHD flow. The code has been parallelized using message passing interface (MPI). The physical units of length and time are set by the mass of the black hole.

Our fiducial simulation is the semi-MAD run. We choose a fixed simulation time $T = 10,000M$ to compare images and spectra. Time-averaged $\dot{m}$ and $\dot{E}$ are found to be nearly constant in radius for the inner $r < 35M$ for SANE, semi-MAD and MAD simulations alike, indicating that inflow and outflow equilibrium is obtained for the regions of interest in this work. In fact, the MAD simulation is in equilibrium up to $r \lesssim 100M$.

4 EMISSION MODELS

4.1 Electron Thermodynamics Models

4.1.1 Electron Evolution Model with Turbulent Heating

All of our simulations also include an electron entropy equation as described in Ressler et al. (2015) (neglecting electron conduction), using the Howes (2010) heating prescription for turbulent heating in collisionless plasmas– appropriate, for example, in the solar wind. We refer to this as the "Electron Evolution Model with Turbulent Heating" (or "Electron Evolution Model" for short).

The Howes (2010) heating function is strongly dependent on plasma $\beta = P_g/P_B$, with a sharp transition between electrons being preferentially heated at $\beta \lesssim 1$ to protons being preferentially heated at $\beta > 1$. A direct consequence is that the relativistically hot electrons are confined to the coronal and jet regions of the simulations while the electrons in the midplane of the disk are non-relativistically cold.

4.1.2 Critical Beta Electron Temperature Model

In an attempt to mimic the behavior of the Electron Evolution Model– without explicitly including turbulent heating in an entropy equation– we construct a post-processing function for the electron-to-total temperature ratio:

$$\frac{T_e}{T_p} = f e^{-\frac{\beta}{\beta_c}}, \tag{1}$$

where $0 < f < 1$ is a constant, and β_c is the critical value of β that approximately sets a maximum β contributing to emission. We call this model the "Critical Beta Electron Temperature Model" (or "Electron Temperature Model" for short). Note $T_p \approx T_{\rm tot} = T_{\rm sim}$ under the assumption that proton cooling is negligible.

This model converges to unique values for the ratio T_e/T_p in the limits $\beta \to 0$ and $\beta \to \infty$ similarly to models in Davelaar et al. (2018) employed by the EHT for M87 in which the ratio of proton-to-electron temperature is bounded by constants $R_{\rm low}$ and $R_{\rm high}$.

4.1.3 Constant Electron Beta Model

Another viable post-processing prescription for the electron temperature is one in which the electron energy density u_e is some fixed fraction of the magnetic energy density u_B. This may be reasonable if magnetic reconnection is the dominant source of electron heating as it is presumed to be in jet regions. This "Constant Electron Beta Model" (or "Constant β_e Model") is described by a single parameter through the relation $\beta_e = P_e/P_B = (\gamma_e - 1)u_e/(b^2/2) = \beta_{e0}$ (constant), or:

$$P_e = \beta_{e0} P_B. \tag{2}$$

where $b^2 \equiv b^\mu b_\mu$.

Note that equipartition of particle and electromagnetic energies corresponds to $\beta_{e0} \sim 1$. Models coupling near-equipartition jets to Sgr A*'s accretion flow have previously been examined in Falcke et al. (1993) and Falcke & Markoff (2000). There, the jets have been invoked to explain the radio emission and, in some models, the higher frequency spectrum.

4.1.4 Magnetic Bias Model

We can generalize the Constant β_e Model so that the electron pressure scales as powers of the magnetic pressure

$$P_e = K_n P_B^n \sim b^{2n} \tag{3}$$

where

$$K_n = K_1 \frac{\langle P_B \rangle}{\langle P_B^n \rangle} = 2^{n-1} K_1 \frac{\langle b^2 \rangle}{\langle b^{2n} \rangle} \tag{4}$$

and $\langle\rangle$ denotes an average over cylindrical radii $2M < R < 20M$ as in Appendix A Table A1. We call this the "Magnetic Bias Model" (or "Bias Model" for short).

Note that $n = 1, K_1 \equiv \beta_{e0}$ corresponds to the Constant β_e Model. By default, for $n \neq 1$, we take $K_1 = 1$ in this work in the interest of space, although there is a priori no strong motivation for a particular value of K.

4.2 Radiative Transport

We compute (mainly 230 GHz) images using the ray-tracing scheme `IBOTHROS` (Noble et al. 2007), which includes the effects of synchrotron emission and absorption, while we compute spectra using the Monte-Carlo-based `GRMONTY` (Dolence et al. 2009), which includes the effects of synchroton emission, absorption, and inverse Compton scattering. For the purposes of radiative transport, we exclude regions of the simulation with $\sigma \equiv b^2/\rho > 1$ where the GRMHD solution becomes less reliable.

Since GRMHD simulations are scale free, for each electron temperature model we choose the physical mass unit such that the flux at 230 GHz matches the 2.4 Jy measurement (Doeleman et al. 2008) (to $< 2\%$). Table 1 lists the resulting mass accretion rate for each of our models. Note that negative accretion rate corresponds to inflow.

Our fiducial viewing angle will be 90° (edge-on disk) and our fiducial observer frequency will be $\nu_{\rm Obs} = 230$ GHz, though we also consider 0° (face on disk), 45° and $\nu_{\rm Obs} = 140$ THz, the latter for comparison with near infrared observations.

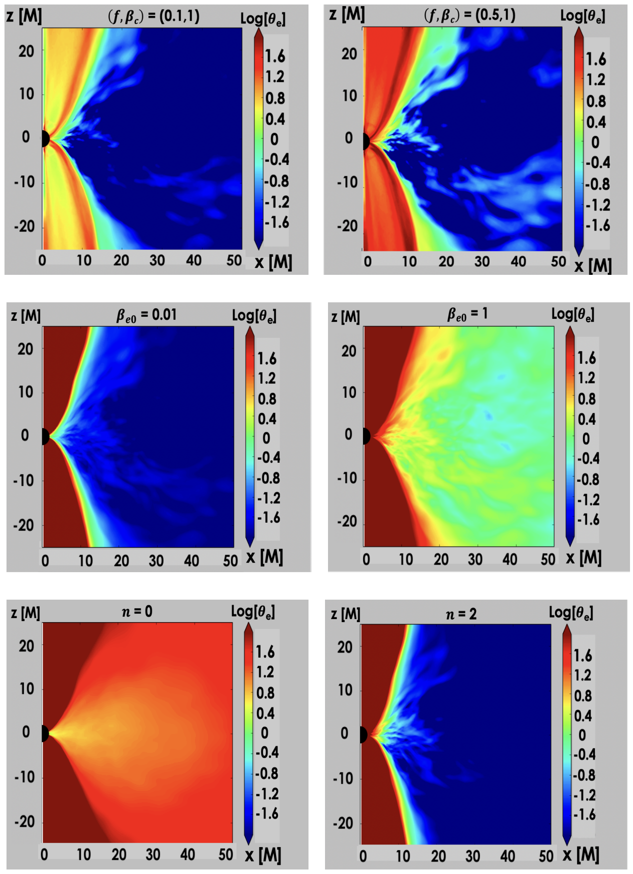

Figure 1. Electron temperature $r\theta$ profiles for the Critical Beta Electron Temperature Model with $(f, \beta_c) = (0.1, 1)$ (Top Left) and $(0.5, 1)$ (Top Right). Also, electron temperature $r\theta$ profiles for Constant β_e Models with $\beta_{e0} = 0.01$ (Middle Left), $\beta_{e0} = 0.1$ (Middle Right), and Bias Models with $n = 0$ (Bottom Left) and $n = 2$ (Bottom Right). The temperature is expressed in dimensionless form $\theta_e = k_B T_e/m_e c^2$.

5 RESULTS

5.1 Electron Temperature Profiles

Figure 1 shows the azimuthally averaged electron temperature distributions in the r-θ plane resulting in each of our models for a few select parameter choices. For Critical Beta Electron Temperature Models, a boundary layer on the disk-jet interface (mild outflow+corona) is the region with highest T_e. This behavior is consistent throughout the parameter space $f \in \{0.1, 0.5\}$ and $\beta_c \in \{0.01, 0.1, 1\}$.

The electron temperature profiles in various Constant β_e Models in the middle panels of Figure 1 are hottest for the strong interior outflow, or "spine," characterized by low density and high magnetization. In Bias Models at the bottom panels of Figure 1, electron temperature is also highest near the coherent, electromagnetically-dominated outflow. Now, however, the radial profile is strongly dependent on the exponent n, which enhances the variation of emission (a function of b) with cylindrical radius in the simulation.

5.2 Electron Evolution Model with Turbulent Heating

5.2.1 Electron Evolution Model Images

The Electron Evolution Model image in Figure 2 shows photon rings around the black hole event horizon and a small outflow: the whispy outflow is visible at radii not exceeding $30M$ and is limb brightened. Asymmetry in the photon ring is apparent, due to Doppler shifts at the edge on viewing angle.

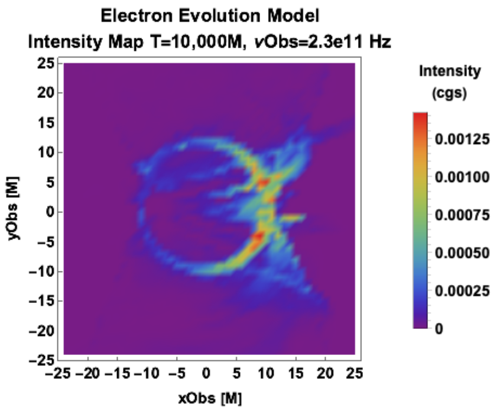

Figure 2. Electron Evolution Model image at 230 GHz.

5.2.2 Electron Evolution Model Spectra

The Electron Evolution Model spectrum is shown in Fig. 3. The infrared bump is well fit, however the model's low frequency slope steepens under the data around 10 GHz, and the model significantly overpredicts the X-ray emission.

Table 1. Mass accretion rate yielding ≈ 2.4 Jy 230 GHz flux for our models. Negative values of mass accretion rate correspond to infall. The monochromatic flux is summed over $50M$ x $50M$ image regions.

Model	Accretion Rate $M_\odot$/yr SANE	semi-MAD	MAD
Electron Evolution with Turbulent Heating	$-2.61 \cdot 10^{-8}$	$-1.70 \cdot 10^{-8}$	$-1.44 \cdot 10^{-11}$
Critical Beta Electron Temperature (f, β_c)			
$(0.1, 0.01)$	$-1.11 \cdot 10^{-7}$	$-1.72 \cdot 10^{-7}$	$-1.90 \cdot 10^{-9}$
$(0.1, 0.1)$	$-8.10 \cdot 10^{-8}$	$-1.16 \cdot 10^{-7}$	$-4.31 \cdot 10^{-10}$
$(0.1, 1.0)$	$-6.92 \cdot 10^{-8}$	$-9.14 \cdot 10^{-8}$	$-2.58 \cdot 10^{-10}$
$(0.5, 0.01)$	$-2.57 \cdot 10^{-8}$	$-3.62 \cdot 10^{-8}$	$-3.11 \cdot 10^{-10}$
$(0.5, 0.1)$	$-1.52 \cdot 10^{-8}$	$-1.13 \cdot 10^{-8}$	$-7.87 \cdot 10^{-11}$
$(0.5, 1.0)$	$-3.93 \cdot 10^{-9}$	$-6.06 \cdot 10^{-9}$	$-2.15 \cdot 10^{-11}$
Constant Electron Beta (β_{e0})			
0.01	$-4.75 \cdot 10^{-9}$	$-2.92 \cdot 10^{-9}$	$-3.14 \cdot 10^{-11}$
0.1	$-3.11 \cdot 10^{-10}$	$-6.28 \cdot 10^{-10}$	$-4.83 \cdot 10^{-12}$
1.0	$-3.90 \cdot 10^{-11}$	$-3.86 \cdot 10^{-10}$	$-1.62 \cdot 10^{-12}$
Magnetic Bias (n)			
0	$-4.04 \cdot 10^{-9}$	$-1.41 \cdot 10^{-9}$	$-1.66 \cdot 10^{-9}$
1	$-3.90 \cdot 10^{-11}$	$-3.86 \cdot 10^{-10}$	$-1.62 \cdot 10^{-12}$
2	$-2.21 \cdot 10^{-11}$	$-4.54 \cdot 10^{-10}$	$-1.95 \cdot 10^{-12}$

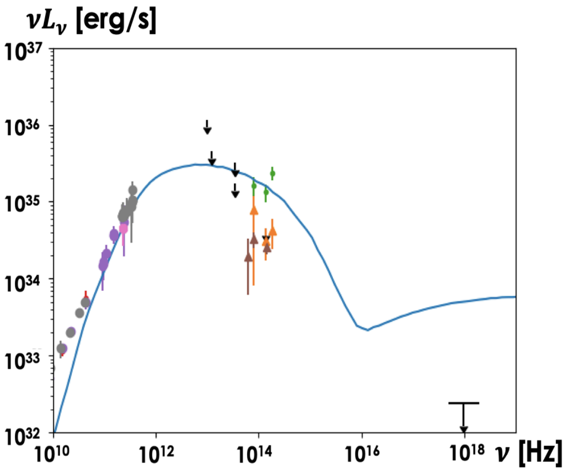

Figure 3. Spectrum generated from the Electron Evolution Model with Turbulent Heating.

5.3 Critical Beta Electron Temperature Model

5.3.1 Electron Temperature Model Images

The images in Fig. 4 show the β_c variation of the Electron Temperature Model for $f = 0.1$ and $f = 0.5$, respectively. For most of the parameter space, the Electron Temperature Model appears to be a fairly uniform projection of the inflow-outflow boundary/coronal region. For the highest values of f and β_c, the images become more asymmetric and the outflow is limited to smaller radii. Optical depth effects are apparent as follows: In the optically thin case, the prescription $T_e = fT_p e^{-\beta/\beta_c}$ at constant β_c has line-of-sight intensity proportional to f; yet the brightness of intensity maps in Fig. 4 are not simple re-scalings of each other as a function of f. This is most noticeable at the highest value $\beta_c = 1$, where the intensity map appears several times more compact and lopsided as we vary f from 0.1 to 0.5.

5.3.2 Electron Temperature Model Spectra

Electron Temperature Model spectra generated with parameter values $(f, \beta_c) = (0.1, 1)$ and $(0.5, 1)$ are shown in Fig. 5. Increasing the overall electron temperature prefactor f at constant β_c is seen to increase the width of the synchrotron peak– reflecting a greater range of emitting temperatures. For $(f, \beta_c) = (0.5, 1)$, the model fits data points over a remarkably broad frequency range: from microwaves to infrared to X-rays. From our parsimonious set of two assumptions regarding high and low β electron temperature behavior, the simple parametrized Electron Temperature Model performs comparably to the full electron evolution calculation. In fact, for $(f, \beta_c) = (0.5, 1)$, the Critical Beta Electron Temperature Model is in better agreement with observations at the high frequency end.

5.4 Constant Electron Beta Model

5.4.1 Constant β_e Model Images

Constant β_e Model images are presented for $\beta_{e0} = 0.01, 0.1$ and 1 in the top and middle panels of Fig. 6. The images are comprised of photon rings surrounded by dimmer filaments. Decreasing the parameter β_{e0} decreases the electron temperature and leads to thinner photon rings and increasing outflow-to-inflow ratio of filamentary emission. In this limit as well, we find increasing asymmetry as the photon ring emission wanes into a narrow crescent on one side.[2] The in-

[2] The images in this paper are rendered in observer coordinates left-right and up-down inverted relative to Ressler et al. (2017) due to implementation of a new imaging pipeline where 90° inclination has the accretion flow approaching on the right and black hole spin pointing down.

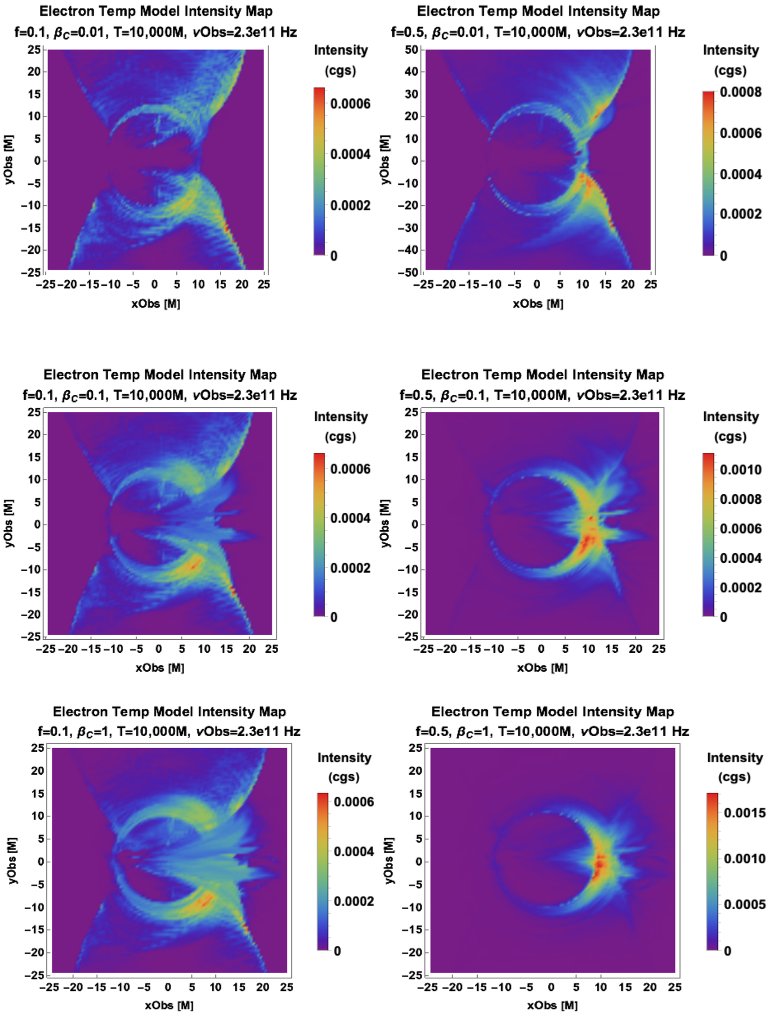

Figure 4. Critical Beta Electron Temperature Model images for $f = 0.1$ (Left Panels) and $f = 0.5$ (Right Panels) for $\beta_c = 0.01$ (Top Panels), $\beta_c = 0.1$ (Middle Panels) and $\beta_c = 1$ (Bottom Panels).

creased asymmetry is quantified in Appendix A2 Table A2; the centroid of the image for $\beta_{e0} = 0.01$ has the furthest lateral displacement for all our models.

5.4.2 Constant β_e Model Spectra

Constant β_e Model spectra for $\beta_{e0} = 0.01$ and 0.1 are shown in Fig. 7 excluding regions $r > 30M$ that are not in equilibrium. These spectra generally reproduce the low frequency slope well, though flatten near the infrared bump– particularly for lower values of the constant β_e. The radio spectra can be explained in the context of the Blandford-Königl model (Blandford & Königl 1979), which demonstrates that helical magnetic fields and constant β_e in regions that are optically thick to synchrotron emission produce radio spectra that are flat in L_ν, consistent with the low frequency emission in Sgr A*. The spectral slope rises in the X-ray, as outflow/jet emission overproduces the high frequency spectrum.

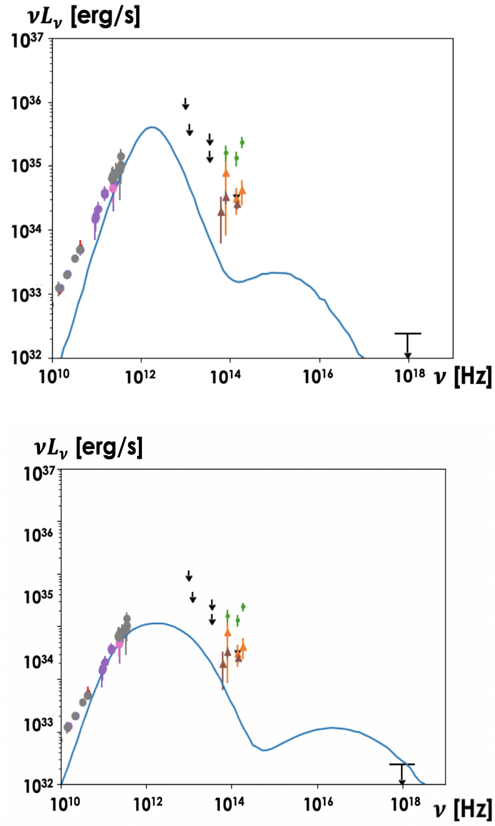

Figure 5. Spectra generated from $(f, \beta_c) = (0.1, 1)$ (Top Panel) and $(0.5, 1)$ (Bottom Panel) Critical Beta Electron Temperature Models.

5.5 Magnetic Bias Model

5.5.1 Bias Model Images

From Eq. 3, it is manifest that the simplest ($n = 0$) Bias Model has constant relativistic electron gas pressure throughout the simulation, in contrast to its expected decrease along the outflow for higher values of n. The image in the bottom left panel of Fig. 6 for $n = 0$ shows extended emission tracing a funnel shape in the jet/outflow region. For $n = 2$, emission becomes dominated by thick photon rings.

For Bias Model images, decreasing n leads to more extended outflow contributions to emission. The Bias and Constant β_e Models have the most drastic variation of image intensity and shape over the observer plane for the models considered in this work.

5.5.2 Bias Model Spectra

Spectra for Bias Models with $n = 0$ and 2 are shown in Fig. 7. The $n = 2$ model dramatically overproduces the emission at IR-X-rays. Both the $n = 0$ and $n = 2$ models do a reasonable job of explaining the low frequency radio emission, which is not surprising since these models are generalizations of the constant β_e model known to explain the radio emission in optically thick AGN jets.

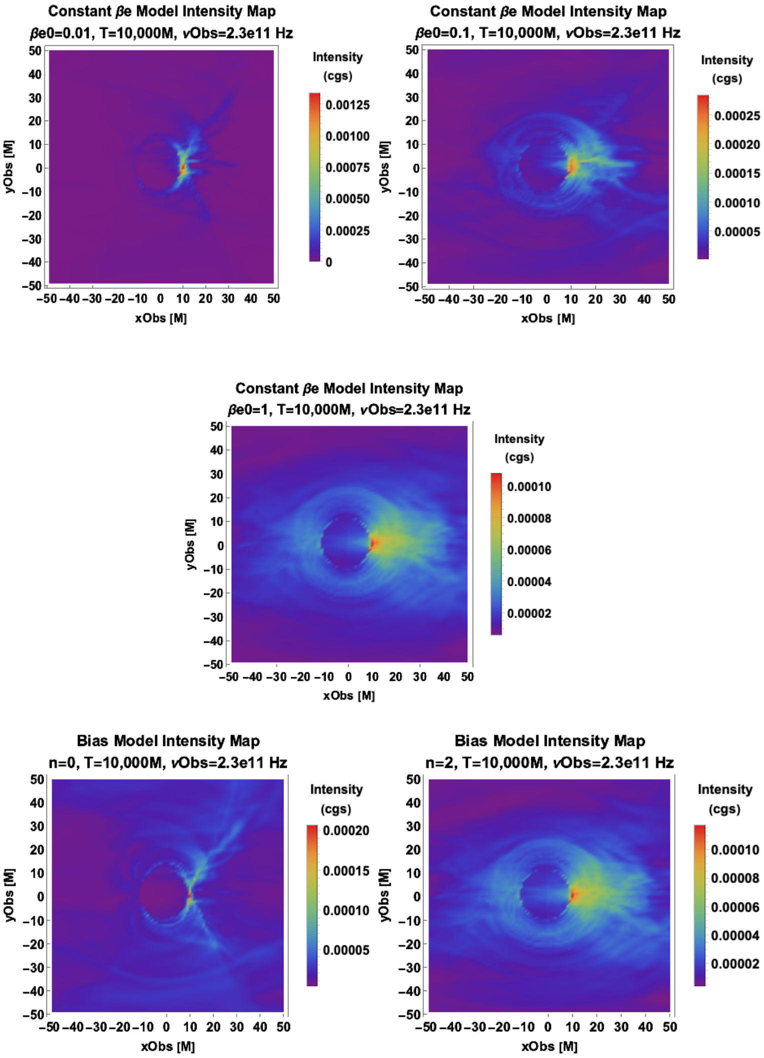

Figure 6. Constant β_e Model image for $\beta e0 = 0.01$ (Top Left) $\beta e0 = 0.1$ (Top Right) and $\beta_{e0} = 1$ (Center), along with Bias Model images for $n = 0$ (Bottom Left) and $n = 2$ (Bottom Right).

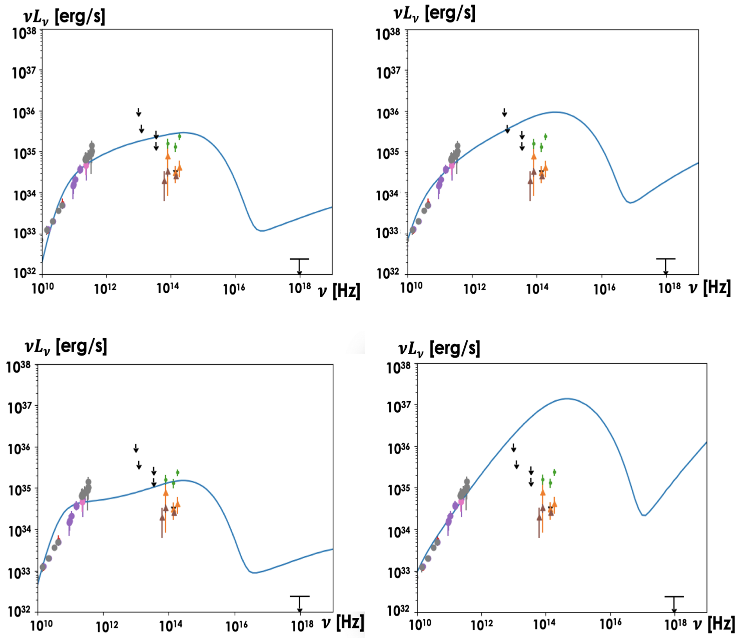

Figure 7. Observed spectra (dots) compared with synthetic model spectra (curves) generated from $\beta_{e0} = 0.01$ Model (Top Left), $\beta_{e0} = 0.1$ Model (Top Right), $n = 0$ Bias Model (Bottom Left) and $n = 2$ Bias Model (Bottom Right).

5.6 EHT and GRAVITY

GRAVITY has provided indications from infrared observations that the Galactic Center inner disk (between $6M$ and $10M$) appears face-on (Gillessen et al. 2017). Fortuitously, a Galactic Center jet may be aimed at small ($\gtrsim 20°$) viewing angle toward us providing 86 GHz (3.5 mm) emission compatible with ALMA observations (Issaoun et al. 2019).

We now compare synthetic EHT-scale (230 GHz) images against GRAVITY-scale (2.2 μm, or 1.4 THz) images for a particular model, $(f, \beta_c) = (0.5, 1)$, in Fig. 8, varying the viewing angle from face-on to edge-on (note, we display these on a common log scale to accentuate features). The face-on disk has smoother variation of intensity with radius at 230 GHz, as it slowly goes from spiral edges to circular at $R \sim 10M$ to the innermost stable circular orbit. At 2.2 μm, the disk appears spiral throughout, punctuated with distinct bright spots. At 45° inclination, the brightest feature at both frequencies is a circular ring with $r \lesssim 15M$. The edge-on view exhibits greater disk asymmetry due to Doppler brightening at 230 GHz, and has a more prominent outflow with more apparent substructure at 2.2 μm.

5.7 SANE vs. SEMI-MAD vs. MAD Simulations

Standard and normal evolution (SANE), magnetically arrested disk (MAD) and semi-MAD simulations represent quite distinct forms of evolution of magnetized accretion flows. The SANE case has the lowest magnetic flux; the MAD case admits the lowest amount of mass accreted by the black hole, as in Table 3. Compared to images ray traced from the fiducial semi-MAD simulation, the SANE and MAD images vary in size and asymmetry in a similar manner with changing parameters in our models. For example, Fig. 9 shows that increasing Critical Beta Electron Temperature Model parameter f from 0.1 to 0.5 takes a relatively symmetric photon ring and extended outflow structure to a compact, asymmetric ring for all three simulations. The same trend holds for increasing β_c from 0.01 to 1. For the $f = 0.5$ models in all three simulations, a disk feature is visible emanating from the bright spot and extending along the projected equatorial plane. It is also noteworthy that the best 10^{11} Hz $< \nu_{\rm Obs} < 10^{19}$ Hz spectrum across simulations (cf. Fig. 10) corresponds to the $(f, \beta_c) = (0.5, 1)$ model in the semi-MAD simulation; however, the MAD simulation for this model generates the best low frequency fit. As for other models, decreasing Constant Electron Beta Model Parameter β_{e0} from 1 to 0.01 changes images from thick photon rings to thin rings + outflows. Decreasing Magnetic Bias Model parameter n from 2 to 0 accentuates the outflow in all 3 simulations, with the key difference being greatest col-

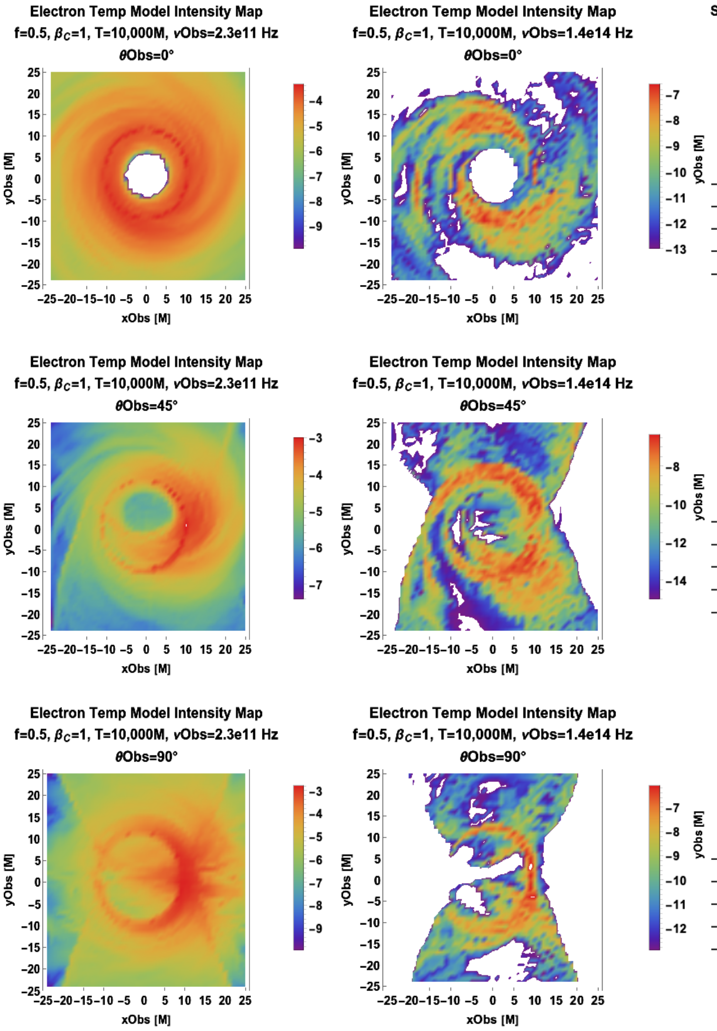

Figure 8. EHT scale (230 GHz, Left) versus GRAVITY scale (140 THz, Right) logplot images of the favored $(f, \beta_c) = (0.5, 1)$ Model. The observer angle varies from $\theta_{\mathrm{Obs}} \approx 0$ to $\frac{\pi}{4}$ to $\frac{\pi}{2}$ from Top to Bottom. These image maps are shown on a log scale in order to accentuate features in the intensity profiles.

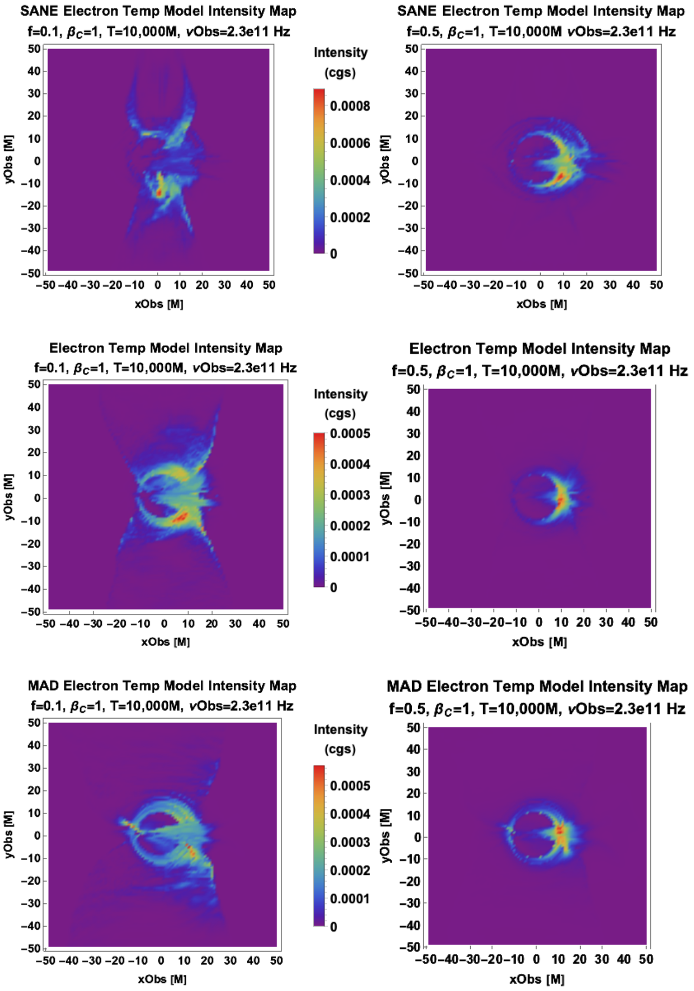

Figure 9. Critical Beta Electron Temperature Model for $f = 0.1$ (Left Panels) and $f = 0.5$ images (Right Panels) for $\beta_c = 1$ SANE (Top Panels), semi-MAD (Middle Panels) and MAD simulations (Bottom Panels).

limation in the SANE simulation. For all simulations and models, inclusion of non-thermal particles could readily increase the IR and X-ray emission.

6 COMPARISON OF MODELS

We now synthesize our results to assess which models are favored by observations, starting with our fiducial semi-MAD simulation.

6.1 Comparison of Images

In the images for the Electron Evolution Model with Turbulent Heating, the emission is concentrated in an asymmetric photon ring, with some some contribution from outflow at small radii. The Critical Beta Electron Temperature Model images have emission smeared out broadly over inflow and outflow at low f or β_c, and approach a compact, asymmetric photon ring for $(f, \beta_c) \to (0.5, 1)$, with even less outflow contribution relative to the Electron Evolution Model. The Constant β_e and Bias Models have drastically varying morphology over the parameter space scanned– from long, extended outflow filaments for the low β_{e0} and low n models, to thick photon rings in the high β_{e0} and high n limits.

The relative asymmetry of model images can be compared using image moments in Appendix A2 Table A2, where models in which most of the flux density emanates from compact regions regions such as $\beta_{e0} = 0.01$ or $(f, \beta_c) = (0.5, 1)$ are shown to have centroids shifted furthest to the right in our fiducial simulation. We make further quantitative comparisons of the images by ascribing emitting region sizes to our intensity maps.

6.1.1 Emitting Region

Given limited instrumental sensitivity, we may only observe the brightest regions around the horizon of Sgr A*. Thus,

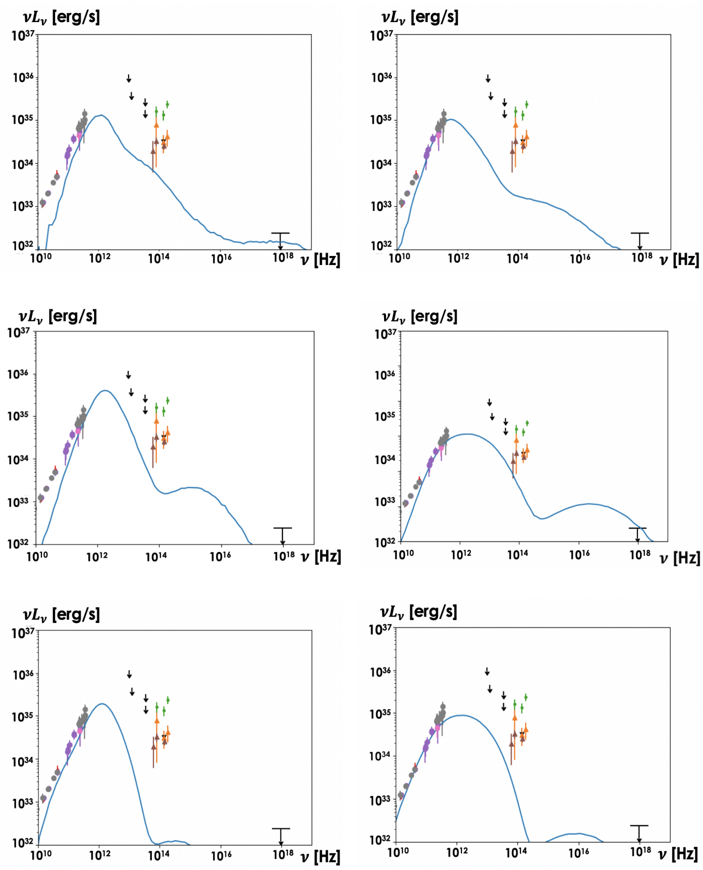

Figure 10. Critical Beta Electron Temperature Model $f = 0.1$ (Left Panels) and $f = 0.5$ spectra (Right Panels) for $\beta_c = 1$ SANE (Top Panels), semi-MAD (Middle Panels) and MAD simulations (Bottom Panels).

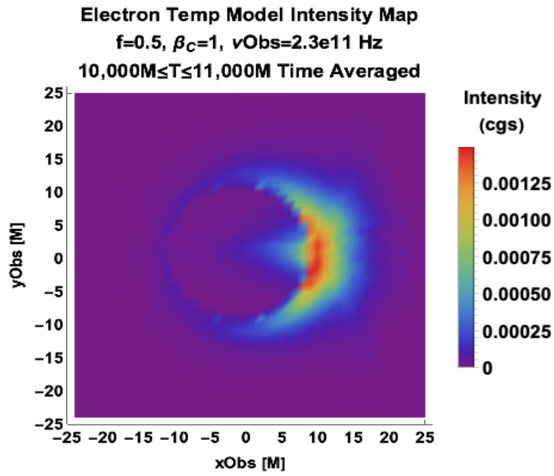

Figure 11. Preferred model ($(f, \beta_c) = (0.5, 1)$) averaged over simulation times $10,000M < T < 11,000M$ at 230 GHz.

it is useful to define emitting regions for our models. The images of the previous section typically have easily distinguishable bright spots with near-maximum intensity. For the Electron Evolution Model with Turbulent Heating, the highest intensity regions are in two spots on the photon ring with $x_{\rm Obs} \approx 8M$ and $y_{\rm Obs} \approx \pm 5M$. For the Critical Beta Electron Temperature Model, there are competing highest intensity locations on the photon ring and outflow until f and β_c are maximal, whence one spot wins out where the photon ring meets the equatorial plane. This spot is also distinctly brightest for all the β_{e0} and n values considered. Relatively bright regions near the intensity maxima appear to become more compact with increasing Critical Beta Electron Temperature Model parameters (f, β_c), more extended with increasing Constant β_e Model parameter β_{e0} and goes from outflow to disk dominated as Magnetic Bias Model parameter n increases.

Note that observational effects such as scattering, the point spread function and instrument-specific cadence tend to wash out image features. While we do not include a model for scattering in this work, we have time-averaged our preferred model in Fig. 11 to reflect uncertainties due to temporal resolution. The time averaged image for the $\sim$ 6h interval $10,000M < T < 11,000M$ is similar to the instant one in Fig. 4 (Lower Right), and the spectral shape does not vary appreciably even over the $\sim$ 12h interval $9,000M < T < 11,000M$, as discussed in Appendix B.

Emitting region sizes defined as the area of the region with intensity at least 20% of maximum intensity are shown in Table 2 (the 10% of maximum emitting region is also reported for comparison). The Event Horizon Telescope has set a FWHM constraint of 37^{+16}_{-10} μas for the intrinsic size of the Sgr A* emitting region interpreted as a 2D Gaussian profile. We define the characteristic length scale of our images as the diameter of the circle whose area equals that of emitting portions with at least at least 0.2 of the maximum spectral intensity (note for an EHT dynamic range of 2 decades of magnitude, $\mathcal{O}(10\%)$ would be the geometric mean of min and max intensity). This Gaussian FWHM extrapolates to $8.2M < D_{>20\%} < 16.2M$, as used in Table 2. For the fiducial simulation, the $\beta_{e0} = 0.01$, $(f, \beta_c) = (0.5, 1)$, Electron Evolution and $n = 0$ Magnetic Bias Models satisfy the observational constraint with $D_{>20\%} = 10.1$, $15.5M$, $15.7M$ and $16.0M$, respectively. The other synthetic image regions considered are more extended, typically by a factor of a few. Note the SANE simulation $\beta_{e0} = 0.01$ Model, MAD simulation $\beta_{e0} = 1$ Model and both of these simulations' Electron Evolution Models also satisfy the EHT size constraint.

6.2 Comparison of Spectra

The Electron Evolution Model with Turbulent Heating fits most of the data near the sub-mm bump. Spectra in models inspired by equipartition (Constant β_e and Bias) are dominated by near-horizon outflow emission. These spectra significantly overproduce frequencies above infrared, even for models satisfying the EHT size constraint in SANE and MAD simulations. For the Bias Model, lower n reduces the falloff of u_e with radius, accounting for flatter radio and X-ray spectra. Spectra in the Critical Beta Electron Temperature Model tend to be dominated by outflow or coronal emission, especially at lower f or β_c, and tend to be more peaked than the data.

Table 2. Characteristic size (diameter of the circle whose area equals that of the region with at least 10%- or 20%-maximum intensity) for our models.

Model	$D_{\geq 10\%}$ (M)			$D_{\geq 20\%}$ (M)		
	SANE	semi-MAD	MAD	SANE	semi-MAD	MAD
Electron Evolution with Turbulent Heating	13.54	21.23	11.26	10.47	15.71	7.23
Critical Beta Electron Temperature (f, β_c)						
$(0.1, 0.01)$	30.20	37.51	52.01	21.12	27.14	36.66
$(0.1, 0.1)$	29.06	36.86	34.76	21.17	26.93	21.81
$(0.1, 1.0)$	30.38	35.52	34.68	20.24	28.42	24.92
$(0.5, 0.01)$	27.03	27.47	35.95	18.95	19.85	16.30
$(0.5, 0.1)$	26.79	23.95	31.17	19.04	18.35	19.23
$(0.5, 1.0)$	26.97	20.21	26.62	20.58	15.50	20.07
Constant Electron Beta (β_{e0})						
0.01	24.24	15.52	25.51	13.68	10.10	16.53
0.1	38.68	46.94	42.64	25.80	25.41	20.77
1.0	66.81	97.67	39.58	44.90	58.40	12.81
Magnetic Bias (n)						
0	39.89	63.09	55.48	24.43	15.99	25.57
1	38.68	97.67	42.64	44.90	58.40	12.81
2	81.41	91.26	104.04	62.32	54.22	49.33

The following summarizes trends appearing upon comparing spectra in different models:

- The Critical Beta Electron Temperature Model reproduces low- and high-energy spectral amplitudes over the $10^{11} - 10^{19}$ Hz frequency domain better than the Constant β_e and Bias Models.
- The radio-IR spectrum is flatter for lower β_{e0} in the Constant β_e Model.
- The radio-IR spectrum is flatter for lower n in the Bias Model.
- Spectra in the Constant β_e and Bias Models appear flatter than spectra in the Critical Beta Electron Temperature Model.

Some of these trends are a consequence of varying mass accretion rate and synchrotron absorption in different models, as discussed below.

6.2.1 *Trends With Mass Accretion Rate*

From Table 1, model families with flatter spectra (Constant β_e and Bias Models) tend to have lower (magnitude) mass accretion rates than the family with steeper spectra (the Critical Beta Electron Temperature Model). This can be explained from the simulation as follows: As $|\dot{m}|$ decreases at fixed flux at 230 GHz, temperature increases and plasma in regions that have not previously been emitting synchrotron radiation begin to emit, broadening the range of emitting temperatures and, in turn, the spectra. This also predicts an anticorrelation between the magnitude of the mass accretion rate and the size of the emitting region in images in optically thin synchrotron models, but optically thick models deviate markedly from this trend.

6.3 Phenomenological Classification

For our fiducial semi-MAD simulation, upon exploration of parameter space, (f, β_c) models tend to outperform the jet-inspired Constant β_e and Bias (n) Models with respect to spectral observations, and often outperform the detailed Electron Evolution Model with Turbulent Heating as well.

With respect to image morphology, observations favor compactness. Though all of our model families can achieve the $D_{>20\%}$ EHT size constraint in appropriate parameter limits, only the two models with the most compact emitting regions, found for $\beta_{e0} = 0.01$ and $(f, \beta_c) = (0.5, 1)$, also satisfy the $D_{>10\%}$ EHT size constraint $12.8M < D_{>10\%} < 20.8M$. It is noteworthy that the highest (f, β_c) pair producing the best spatial fit for the Critical Beta Electron Temperature Model also provides the best overall spectral fit, giving us indication that the image and spectral properties are correlated. Moreover, image compactness is related to image shape in our models, as the lowest $\beta_{e0} = 0.01$ providing the best (smallest) emitting region size has image morphology resembling the asymmetric crescent from the $(f, \beta_c) = (0.5, 1)$ Model.

Upon a scan of model parameter space for our fiducial simulation, we find that images tend to aggregate into (at least) 4 broad categories, which are closely tied to spectra as well:

I.) Thin, Compact, Asymmetric Photon Ring/Crescent
This image morphology is exhibited for the Electron Evolution Model with Turbulent Heating and in parameterized models with $(f, \beta_c) \in \{(0.5, 0.1), (0.5, 1)\}$ or $\beta_{e0} = 0.01$. The concomitant spectra are the best fit across our models, with the largest deviation coming from the $\beta_{e0} = 0.01$ Model's very flat spectrum in the IR band and mild X-ray excess.

II.) Inflow-Outflow Boundary + Thin Photon Ring
This image morphology is exhibited in models with $(f, \beta_c) \in \{(0.1, 0.01), (0.1, 0.1), (0.1, 1), (0.5, 0.01)\}$, and is accompa-

nied by the steepest spectra, sharply peaking near the IR bump.

III.) Thick Photon Ring
This image morphology is exhibited in the Constant β_e Model with $\beta_{e0} \in \{0.1, 1\}$, and the Bias Model with $n = 2$, and is accompanied by spectra with large X-ray excesses (and a flat overall spectrum for $\beta_{e0} = 0.1$).

IV.) Extended Outflow
Occurring in the $n = 0$ Bias Model, this image morphology is linked to a flat overall spectrum with X-ray excess.

It is noteworthy that dominant image features are closely linked with dominant spectral features, and that these associations form the basis for distinct classes into which models governed by related physics– albeit different parameterizations thereof– can be identified.

6.3.1 *SANE vs. SEMI-MAD vs. MAD Simulation Comparison*

As we consider simulations outside of the fiducial simulation, new image morphologies emerge. For example, for the SANE simulation, the $(f, \beta_c) = (0.1, 1)$ Model has a distinctly helical outflow intensity map and a remarkably good spectral fit for all but the lowest frequencies (cf. Figs. 9 and 10). Furthermore, it is notable that some of our models become similar to our favored $(f, \beta_c) = (0.5, 1)$ Model in appropriate limits. In particular, as β_{e0} goes from 1 to 0.01 in the Constant β_e Model, intensity maps become more confined to small cylindrical radius and asymmetric for SANE, semi-MAD and MAD cases alike; and, for the MAD simulation, closer spectral fits are produced for the microwave, IR and (especially) X-ray bands. The theoretical advancement of a single model unifying emission characteristics of accretion flow, corona and outflow using a single simulation and small set of parameters would enable us to directly identify observed features with plasma and emission physics of different AGN components.

7 CONCLUSIONS AND FUTURE DIRECTIONS

We have used two simple classes of parametric emission prescriptions– the turbulent-heating-based Critical Beta Electron Temperature Model $T_e = fT_p e^{-\beta/\beta_c}$ and the equipartition-based Constant Electron Beta/Magnetic Bias Models $P_e = K_n P_B^n$, ($\beta_{e0} \equiv K_1$ for $n = 1$)– to explore a wide range of possible models for the images and spectra in the inner tens of gravitational radii around the supermassive black hole at the Galactic Center. One of our models, $(f, \beta_c) = (0.5, 1)$, input into our fiducial semi-MAD simulation, is observationally favored for Sgr A* due to its agreement with respect to the spectrum, emitting region compactness and asymmetry. We stress that both observationally preferred images and spectra are associated with emission concentrated in a bright, crescent-shaped portion of the photon ring near the horizon, and that forthcoming EHT and GRAVITY data will further constrain our models.

It is worth noting our intuitive one- and two-parameter models span new electron physics beyond what has been previously explored, and promise to bear upon AGN beyond Sgr A*. By surveying synthetic images and spectra in other parts of model parameter space, we may isolate the emission physics underlying particular observational phenomena. We summarize these results as follows.

7.1 Images Summary

Synthetic 230 GHz intensity maps on the scale of tens of gravitational radii appear:

- Dominated by the inflow/outflow interface for the Critical Beta Electron Temperature Model
- More compact and asymmetric with increasing f or β_c
- Mixed with outflow/near-horizon photon ring emission for the Constant β_e and Bias Models
- More concentrated around near-horizon-circulating photon rings for increasing β_{e0} and increasing n

7.2 Spectra Summary

In comparison to the data, our parameterized synthetic 10^{11} Hz $< \nu < 10^{19}$ Hz spectra have:

- More peaked slopes fairly consistent with the sub-mm bump but underproducing the low frequency tail for the Critical Beta Electron Temperature Model
- Fairly consistent low frequency slope but flatter peak and overproduction of low and (especially) high frequency emission for the Constant β_e Model
- Consistent low frequency slope but broader peak and (in some cases vast) overproduction of high frequency emission for the Bias Model

The steep radio spectra seen in the Electron Temperature Model is characteristic of emission from an adiabatically expanding coronal outflow, in which temperature rapidly declines in radius. The flatter radio spectra from the Constant β_e and Bias prescriptions are due to contributions from the highly magnetized outflow and the dependence of the latter emission functions exclusively on P_B. Although these latter models can explain many features of jets/outflows (including Sgr A*) such as Doppler beaming, knots and other magnetic field substructure, we have shown that they do not accurately describe the inner regions of discs/jets around Sgr A* (and perhaps, by analogy, other systems).

7.3 Future Directions

Sgr A* viewed at 1.3 mm has exhibited intrahour variability (Johnson et al. 2015) in the inner $\sim 6r_g$ around a black hole whose Schwarszchild-radius-light-crossing-time is 44 s. In the future, it would be valuable to produce light curves in the simulations replicating the observational cadence and understand which range of models is most consistent with the observed variability. We may also add polarization maps to our pipeline to test whether electromagnetically dominated emission models in simulations with ordered magnetic field substructure, e.g., helical Blandford-Königl outflows, can help explain observations of a high degree of linear polarization in AGN cores.

The "observing" simulations methodology is a key link between ever-advancing simulations and observations of the central engines of JAB systems. The EHT serves as a timely testbed for our emission models that aim to unite simulations and observations. The next works planned in this "'Observing' JAB Simulations" series are applications to the prominent jets in the giant elliptical galaxy M87 and the highly variable quasar 3C 279. Other EHT target sources to be observed– and possibly, "observed"– in the future include: Cen A, NGC 1052 and OJ 287.

ACKNOWLEDGEMENTS

This work was supported in part by NSF grants AST 13-33612 and AST 1715054, Chandra theory grant TM7-18006X from the Smithsonian Institution, and a Simons Investigator award from the Simons Foundation. This work was made possible by computing time granted by UC Berkeley on the Savio cluster. RA carried out part of this work supported by the California Alliance and Simons Foundation and the remainder of this work at the Black Hole Initiative at Harvard University, which is supported by a grant from the John Templeton Foundation. SR was supported in part by the NASA Earth and Space Science Fellowship during part of the duration of this work.

REFERENCES

Abuter R., et al., 2019, arXiv e-prints,
Anantua R., Blandford R., Tchekhovskoy A., 2018, Galaxies, 6
Blandford R., Anantua R., 2017, in Journal of Physics Conference Series. p. 012023 (arXiv:1705.03119), doi:10.1088/1742-6596/840/1/012023
Blandford R. D., Königl A., 1979, ApJ, 232, 34
Blandford R. D., Znajek R. L., 1977, MNRAS, 179, 433
Bower G. C., et al., 2015, ApJ, 802, 69
Chael A., Rowan M., Narayan R., Johnson M., Sironi L., 2018, MNRAS, 478, 5209
Chan C.-K., Psaltis D., Özel F., Narayan R., Saḑowski A., 2015, ApJ, 799, 1
Davelaar J., Mościbrodzka M., Bronzwaer T., Falcke H., 2018, A&A, 612, A34
Doeleman S. S., et al., 2008, Nature, 455, 78
Dolence J. C., Gammie C. F., Mościbrodzka M., Leung P. K., 2009, ApJS, 184, 387
Event Horizon Telescope Collaboration et al., 2019a, ApJ, 875, L1
Event Horizon Telescope Collaboration et al., 2019b, ApJ, 875, L5
Falcke H., Markoff S., 2000, A&A, 362, 113
Falcke H., Mannheim K., Biermann P. L., 1993, A&A, 278, L1
Fish V. L., et al., 2011, ApJ, 727, L36
Fishbone L. G., Moncrief V., 1976, ApJ, 207, 962
Gammie C. F., McKinney J. C., Tóth G., 2003a, The Astrophysical Journal, 589, 444
Gammie C. F., McKinney J. C., Tóth G., 2003b, ApJ, 589, 444
Gillessen S., et al., 2010, in Optical and Infrared Interferometry II. p. 77340Y (arXiv:1007.1612), doi:10.1117/12.856689
Gillessen S., et al., 2017, ApJ, 837, 30
Gravity Collaboration et al., 2018, A&A, 615, L15
Howes G. G., 2010, MNRAS, 409, L104
Issaoun S., et al., 2019, ApJ, 871, 30
Johnson M. D., et al., 2015, Science, 350, 1242
Lu R.-S., et al., 2018, ApJ, 859, 60
Mahadevan R., Quataert E., 1997, ApJ, 490, 605
Mościbrodzka M., Falcke H., 2013, A&A, 559, L3
Mościbrodzka M., Gammie C. F., Dolence J. C., Shiokawa H., Leung P. K., 2009, ApJ, 706, 497
Mościbrodzka M., Falcke H., Shiokawa H., Gammie C. F., 2014, A&A, 570, A7
Neilsen J., et al., 2013, ApJ, 774, 42
Noble S. C., Leung P. K., Gammie C. F., Book L. G., 2007, Classical and Quantum Gravity, 24, S259
Özel F., Psaltis D., Narayan R., 2000, ApJ, 541, 234
Porth O., Olivares H., Mizuno Y., Younsi Z., Rezzolla L., Moscibrodzka M., Falcke H., Kramer M., 2017, Computational Astrophysics and Cosmology, 4, 1
Ressler S. M., Tchekhovskoy A., Quataert E., Chandra M., Gammie C. F., 2015, MNRAS, 454, 1848
Ressler S. M., Tchekhovskoy A., Quataert E., Gammie C. F., 2017, MNRAS, 467, 3604
Sądowski A., Narayan R., McKinney J. C., Tchekhovskoy A., 2014, MNRAS, 439, 503
Shcherbakov R. V., Penna R. F., McKinney J. C., 2012, ApJ, 755, 133
Sądowski A., Wielgus M., Narayan R., Abarca D., McKinney J. C., Chael A., 2017, MNRAS, 466, 705
Tchekhovskoy A., Narayan R., McKinney J. C., 2011, MNRAS, 418, L79
White C. J., Stone J. M., Gammie C. F., 2016, ApJS, 225, 22
Yuan F., Markoff S., Falcke H., 2002, A&A, 383, 854

APPENDIX A: TABLES

A1 Magnetic Bias Model Normalization Constant

For the Bias Model, the electron gas pressure P_e is prescribed to scale as powers n of the magnetic pressure P_B, requiring a magnetic-to-gas pressure conversion factor with units of pressure to power $1-n$. Table A1 provides this factor by imposing a normalization condition in the semi-MAD simulation that the numerical average of P_B^2 equals that of $K_n P_B$ in the region between concentric cylindrical surfaces at $R = r_\rho = 1.89M$ and $R = 20M$, as well as $50M$ for comparison. An alternative normalization region in which the averaged is take over annuli on the equatorial plane with the height of one simulation pixel produces similar results. Since the averages are similar for our different choices of region geometry and extent, we consider our normalization approach robust.

Table A1. Average values $\langle b^N \rangle$ from cylindrical radii $R = r_\rho = 1.87M$ to $R_{\max} \in \{20M, 50M\}$.

N	Avg. out to $R_{\max} = 20M$	Avg. out to $R_{\max} = 50M$
1	0.0064	0.0023
2	0.00011	1.75e-05
3	5.52e-06	7.22e-07
4	4.63e-07	5.95e-08
5	4.57e-08	5.87e-09
6	4.89e-09	6.29e-10

A2 Statistical Analysis: Moments

We may make quantitative our comparison of the disparate array of images generated from distinct physical processes by a comparison of statistical moments:

$$M_{n_1,n_2} = \sum_{i,j} x_i^{n_1} y_j^{n_2} I(x_i, y_j) \tag{A1}$$

First and second order image moments (centroid and gyroradius) for $-50M < x, y < 50M$ 230 GHz images in key models are presented in Table A2. The centroid of image intensity is right-offset, arising from asymmetric Doppler boosting of the accretion flow. However, it remains within the narrow band between $5M < x < 10M$ and $-M < y < 3M$. The centroid right offset is consistent with the apparent mirror asymmetry in synthetic image brightness, especially in models producing a prominent bright spot on the inner right edge of the disk. The higher moment gyroradius, including standard deviation, has greater variation across models due to contributions from larger radii emitting segments generated from low n or β_{e0} portions of Constant-β_e/Bias Model parameter space.

Table A2. Images moment comparison of 1st and 2nd moments for $-50M < x, y < 50M$ at 230 GHz for key models.

Model	Centroid $\left(\frac{M_{10}}{M_{00}}, \frac{M_{01}}{M_{00}}\right)$	Gyroradius $\left(\sqrt{\frac{M_{20}}{M_{00}}}, \sqrt{\frac{M_{02}}{M_{00}}}, \sqrt{\frac{M_{20}+M_{02}}{M_{00}}}\right)$
Electron Evolution with Turbulent Heating	$(6.56M, -0.15M)$	$(9.96M, 11.56M, 15.26M)$
Critical Beta Electron Temperature (f, β_c)		
$(0.1, 0.01)$	$(5.18M, 1.41M)$	$(11.76M, 20.58M, 23.70M)$
$(0.1, 0.1)$	$(5.25M, 1.65M)$	$(10.70M, 16.92M, 20.02M)$
$(0.1, 1.0)$	$(5.45M, 1.40M)$	$(10.39M, 14.31M, 17.69M)$
$(0.5, 0.01)$	$(6.36M, 2.91M)$	$(11.51M, 18.80M, 22.04M)$
$(0.5, 0.1)$	$(8.13M, 1.80M)$	$(10.81M, 10.53M, 15.09M)$
$(0.5, 1.0)$	$(8.61M, 1.17M)$	$(10.78M, 7.93M, 13.38M)$
Constant Electron Beta (β_{e0})		
0.01	$(9.02M, 1.92M)$	$(16.44M, 21.41M, 26.99M)$
0.1	$(8.47M, -0.65M)$	$(24.51M, 22.55M, 33.31M)$
1.0	$(5.32M, 0.24M)$	$(27.32M, 23.24M, 35.86M)$
Magnetic Bias (n)		
0	$(5.50M, -0.14M)$	$(26.44M, 30.05M, 40.02M)$
1	$(5.32M, 0.24M)$	$(27.31M, 23.24M, 35.86M)$
2	$(5.76M, -0.62M)$	$(26.85M, 22.86M, 35.26M)$

APPENDIX B: TIME AVERAGING

In the main body of the text, we compared models at a fiducial time $T = 10,000M$ in which the simulation flow is in steady state. Given the 22s light crossing time of Sgr A*'s gravitational radius, variability challenges EHT's temporal imaging capacity for Sgr A*– and all but the most massive black holes. Image variability on roughly hourly timescales is apparent for our preferred model. Though features such as bright spots are seen to move around, the Type II morphology is stable throughout, as it is for the time averaged image in Fig. 11. The spectrum also appears stable as hourly timescales, as it does not change perceptibly for logarithmically and linearly sampled times from $9,000M < T < 11,000M$.

This paper has been typeset from a TEX/LATEX file prepared by the author.